A Novel Dexterous Steerable Catheter Robot System: Design, Modeling and Evaluation

Yonggan Yan, Shuxiang Guo, *Fellow, IEEE*, Haikuo Shen, Bin Wang, Mingchao Ding

***Abstract*—Vascular interventional surgery (VIS) robots still face limitations in enhancing treatment quality. The primary challenges come from the accurate morphology control and miniaturization of the distal instruments. To address these issues, a novel 4 degrees of freedom steerable catheter robotic system is developed. The catheter is composed of two segments continua connected in series. By actuating the two segments independently, the distal end of the catheter has both position and wide-range orientation control capabilities. To accurately estimate the continuum deformation, an improved tendon tension propagation model considering the path friction is proposed. Then a continuum morphology estimation model is derived cell by cell based on the chain beam assumption. Based on the estimation model, the kinetostatic model is established and a model-based nonlinear numerical solution method is developed to obtain the inverse solution of the actuation space. Experimental results demonstrate that the improved tendon tension propagation model reduces the control errors in position and orientation by 45.6% and 57.6% respectively compared with the simplified model. Additionally, the dexterity and operability of the robotic system are demonstrated by 4 navigation experiments.**

***Index Terms*—Steerable catheter, surgical navigation, multi-segment continuum, vascular interventional robot.**

I. Introduction

LEADER-FOLLOWER vascular interventional surgery (VIS) robot addresses the defects of surgeons being exposed to X-ray radiation and wearing heavy lead clothes [1]. However, most existing VIS robots still use conventional interventional instruments. The structure redundancy limits the flexibility of the instrument, and also makes the surgical success rate and efficiency of the robot-assisted VIS show no obvious improvement compared to conventional interventional surgery. Fig. 1(a,b) display the 3D model reconstructed from the real aortic arch and coronary artery of an adult, as well as their statistical morphological characteristics [2], [3]. The aortic arch is an important path for the diagnosis and treatment of neurovascular and coronary artery diseases. It is divided into three types according to the position of the carotid artery branches relative to the top of the aortic arch, as shown in Fig. 1(a). Types I, II, and III exhibit increased arch heights and difficulty in superselective [4]. Compared with the aorta, the entrance diameters of the carotid and coronary arteries are significantly reduced by 60%∼88%, and the entrance orientations vary greatly. Surgeries require surgeons to have skilled catheter operation techniques, and even specific surgeries may involve trial and error of multiple pre-plasticized catheters, which increases the operation time and endangers the patient's life. In addition, Fig. 1(b) shows that the coronary artery distal vessel diameter is less than 2 mm, which limits the size of interventional instruments. Therefore, to improve the success rate and efficiency of surgery, it is urgent to develop a miniaturized steerable catheter with accurate control of distal position and orientation.

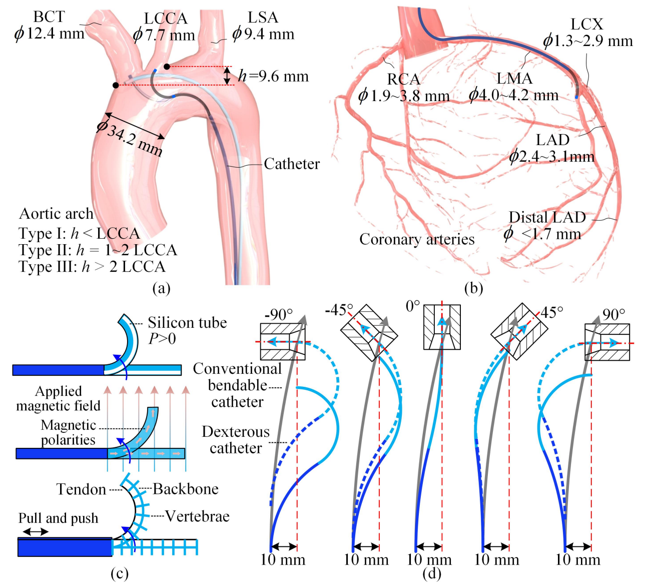

Fig. 1. Two typical vascular features in the human vascular network and various steerable catheters. (a) Average sizes of the aortic arch in adults [2], Brachiocephalic trunk (BCT) 12.4±2.1 mm, Left common carotid artery (LCCA) 7.7±1.2 mm, Left subclavian artery (LSA) 9.4±1.4 mm. h represents the height from the top of the aortic arch to the origin of the brachiocephalic trunk. (b) Average sizes of the coronary artery [3], Right main artery (RCA) 1.9∼3.8 mm, Left main artery (LMA) 4.0∼4.2 mm, Left circumflex branch (LCX) 1.3∼2.9 mm, Left anterior descending artery (LAD) 2.4∼3.1 mm, Distal LAD <1.7 mm. (c) Steerable catheters using different actuation methods. (d) The dexterous steerable catheter.

Steerable continuum robots hold highly promise for use in tortuous environments due to their active bending and structural compliance. Depending on the actuation method,

Manuscript received: March 3, 2025; Revised: June 3, 2025; Accepted: July 2, 2025. This paper was recommended for publication by Editor Yong-Lae Park upon evaluation of the Associate Editor and Reviewers' comments. This paper was supported by the National Natural Science Foundation of China (61703305), and by National High-tech Research and Development Program of China (2015AA043202). (Corresponding author: Shuxiang Guo.)

Y. Yan is with the School of Mechanical, Electronic and Control Engineering, Beijing Jiaotong University, Beijing 100044 and also with Aerospace Center Hospital, School of Life Science, Beijing Institute of Technology, Beijing 100081, China.

S. Guo is with the Department of Electronic and Electrical Engineering, Southern University of Science and Technology, Shenzhen, Guangdong 518055, China, and also with Aerospace Center Hospital, School of Life Science and the Key Laboratory of Convergence Medical Engineering System and Healthcare Technology, Ministry of Industry and Information Technology, Beijing Institute of Technology, Beijing 100081, China (e-mail: guo.shuxiang@sustech.edu.cn).

H. Shen is with the School of Mechanical, Electronic and Control Engineering, Beijing Jiaotong University, Beijing 100044, China.

B. Wang and M. Ding are with the Department of Peripheral Vascular Intervention, Aerospace Center Hospital, School of Life Science, Beijing Institute of Technology, Beijing 100081, China.

Digital Object Identifier (DOI): see top of this page.

they are mainly divided into tendon driven continuum robots (TDCRs) [5], [6], magnetic continuum robots (MCRs) [7], [8], and pneumatic continuum robots (PCRs) [9], [10], as shown in Fig. 1(c). MCRs integrate small-scale permanent magnets or soft magnet at the end, which can respond to the external magnetic field and bend controllably. PCRs typically embed an elongated cylindrical inflatable bladder eccentrically within an elastic sheath. When inflated, the bladder expands one side of the sheath, causing the robot to bend. However, potential gas leak poses a significant threat to the safety of VIS. TDCRs typically consist of an axial backbone, vertebrae and tendons located within the vertebral openings. The tendons, when pulled or pushed, generate a torque on the backbone, resulting in bending. The high control accuracy and miniaturization of the TDCR make it hold substantial potential for application in VIS. The above steerable catheters for VIS often focus on the bending ability of the tip, while ignoring the position and orientation decoupling control capability. Fig. 1(d) shows a two-segment dexterous catheter. At the same radial offset position, the dexterous catheter (blue lines) has independent orientation adjustment capabilities compared to the conventional bendable catheter (gray lines), which enables the catheter to have superior accessibility for directional branches in wide spaces, such as the aortic arch and heart ventricule.

Accurate kinematics modeling and motion control of multi-segment continuum remain challenging. The accumulation of modeling errors in each segment of the continuum reduces the control accuracy of the end effector. Assuming no friction, the piecewise constant curvature (PCC) assumption is widely applied to kinematics modeling of the TDCRs [11]. In practical applications, the influence of tendon friction on the motion control accuracy cannot be ignored. Therefore, the complementary modeling that considers inherent tendon path friction should be further investigated, as some studies have shown that tendon friction plays an important role in kinematics accuracy [12], [13]. However, existing continuum modeling methods considering tendon path friction often simplify the static force direction of the tendon and ignore the impact of the assumption on the accuracy of continuum morphology estimation. In the case of significant deformation or multi-segment continuum, the simplified assumption will lead to insufficient control accuracy of the continuum distal end [14]. In this article, the main contributions are summarized as follows.

1) A novel dexterous 4 degrees of freedom (DoFs) steerable catheter robotic system is developed, and the diameter of the catheter can reach sub-millimeter level, which effectively improves the flexible control capability of the distal end and thus reduces the surgical difficulty.
2) Incorporating the path friction, a tendon tension propagation model is improved. By relaxing the assumption of the normal force direction, the improved model maintains high accuracy in large deformation and two-segment continuum motion control.
3) Morphology estimation-based kinetostatic model of the multi-segment continuum are derived, and a model-based numerical solution method is designed.

The rest of this paper is organized as follows. Section II introduces the developed steerable catheter robotic system; Kinetostatic model is established in Section III; The experimental validation is performed in Section IV. Finally, Section V concludes this article.

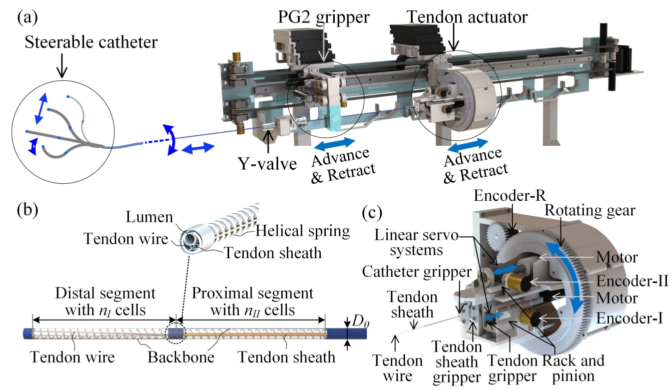

Fig. 2. Designed TDSCR with 4 DoFs. (a) Overview of the TDSCR. (b) Steerable catheter mechanism. (c) Design of the tendon actuator.

II. Mechatronics System Design and Development

As displayed in Fig. 2(a), a novel tendon driven steerable catheter robotic system (TDSCR) for VIS is proposed. It mainly consists of the steerable catheter, tendon actuator, PG2 gripper [15], and control system. The steerable catheter consists of two segments continua located in a plane as displayed in Fig. 2(b). Each segment is mainly composed of a helical spring, an elastic backbone, and a tendon. The backbone is fixedly connected to each turn of the spring. The tendon passes through the spring, and one end is fixed to the end turn of the spring. When the tendon is pulled and pushed, the three parts form a quasi-static force equilibrium state. Then the continuum bends to the right and left. The helical spring not only guides the tendon as the vertebrae, but also effectively supports radial loads. The tendon, tendon sheath, and catheter drive cavity are nested layer by layer. The tendon sheath that can accommodate the tendon of the distal segment is used as the tendon of the proximal segment. The tendon sheath transmitting the driving tension of the proximal segment supports reverse axial forces for the distal tendon, thereby counteracting the deformation caused by the distal segment's driving force on the proximal segment. This mechanism realizes the decoupling of the two continua from the drive space to the motion space. The distal segment backbone and the proximal segment backbone are soldered to the spring at 180° intervals. The diameter of the backbone determines the stiffness and the rated tendon tension. The thin backbone in the distal segment is friendly to the vascular environment. The soft catheter tip can avoid excessive contact force and ensure surgical safety. The thicker backbone in the proximal segment has a higher inherent stiffness and provide stable support for the distal segment. A lumen is reserved for delivering drugs or instruments.

The steerable catheter is controlled by the tendon actuator, and its mechanical structure is shown in Fig. 2(c). The displacement of the tendon and tendon sheath is accurately controlled by two linear servo systems. Encoder-I and Encoder-II, with an accuracy of 1 um, measure the displacements of the lead screw nuts through gear rack transmission. Encoders and

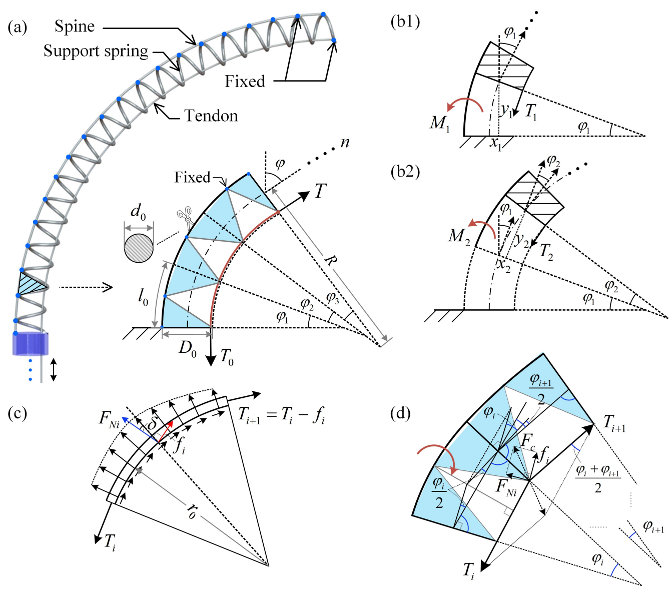

Fig. 3. Continuum configuration and deformation analysis. (a) Continuum equivalent simplification. (b) Euler-Bernoulli beam assumption on quasi-static continuum. (c) Equilibrium of an infinitesimal area between tendon and spring. (d) Tension propagation modeling with friction.

motors establish two position closed-loop systems respectively. The two linear servo systems are fixedly connected to a rotating gear driven by a motor. A rotation servo system is built based on Encoder-R. The PG2 gripper is our previous related works [15]. The two parallel fingers can reach, grasp, and twist small objects, as shown in Fig. 2(a). The finger pulp integrated force sensors detects the inserting force, grasping force, and the sliding state of the instrument between the fingers. Since the flexible catheter body is easy to deflect during inserting, the advance and twist is performed by the PG2 gripper near the Y-valve. The tendon actuator follows these manipulations actively. When advancing the catheter, it is important to ensure dynamic synchronization of the gripper and the tendon actuator, otherwise it will interfere with the insertion force measurement. Finally, the steerable catheter tip has 4 active DoFs.

III. Continuum Modeling

A. Modeling Assumptions

The sagittal plane of a continuum is shown in Fig. 3(a). Each turn of the spring and the backbone are combined into a stable triangular cell. Here, the continuum is simplified into a 2D lumped parameter model consisting of many congruent cells in cascade. The base of the each triangle is fixed to the backbone. Without loss of generality, the following are four assumptions for the model:

A1) Friction forces and normal forces acting on the tendon are concentrated forces. The tension difference between adjacent contact points is equal to the friction [12].

A2) Friction coefficient is constant for the same contact pair.

A3) The spring is dense enough that the curvature at the bottom corner of the cell can represent the cell curvature.

A4) The continuum configuration is divided into multiple equal length parts by lines perpendicular to the tendon. Each part is an Euler-Bernoulli beam.

B. Tendon Tension Propagation Model

Fig. 3(a) displays the lumped parameter model, with a backbone diameter of d_0, a pitch of l_0, a outer diameter (OD) of D_0. The orientation angle of the i-th cell is φ_i, and the tension is T_i. The force analysis of the first cell is shown in Fig. 3(b1). Since the forces on the 2-nd to n-th cells are internal forces, they are regarded as a whole and not considered. Assuming A4, the moment of the first cell M_1 is written as:

$$M_1 = T_1 D_0. \tag{1}$$

The root of the backbone is subjected to an axial force and a moment. According to the Euler-Bernoulli equation:

$$\frac{\mathrm{d}\varphi}{\mathrm{d}s} = \frac{M_1}{EI}, \tag{2}$$

where ds represents the infinitesimal beam element, E represents the Young's modulus of the backbone material, and I is the moment of inertia of the backbone's cross-section about the neutral axis. The first deformation angle is obtained by separating the variables and integrating:

$$\int^{\varphi_1} \mathrm{d}\varphi = \int_0^{l_0} \frac{M_1}{EI} \mathrm{d}s, \tag{3}$$

$$\varphi_1 = \frac{M_1 l_0}{EI}. \tag{4}$$

By the differential chain rule, substitute $\frac{\mathrm{d}x}{\mathrm{d}s} = \sin\varphi$ into (2):

$$\frac{M_1}{EI} = \frac{\mathrm{d}\varphi}{\mathrm{d}x}\frac{\mathrm{d}x}{\mathrm{d}s} = \frac{\mathrm{d}\varphi}{\mathrm{d}x}\sin\varphi. \tag{5}$$

where x represents the lateral deformation. By separating the variables and integrating, x_1 is written as:

$$x_1 = \frac{EI}{M_1}(-\cos\varphi_1 + 1) \tag{6}$$

Similarly, the longitudinal position y_1 can be obtained:

$$y_1 = \frac{EI}{M_1}\sin\varphi_1 \tag{7}$$

Given the tendon tension, we can calculate the relative deformation angle and end position of the i-th cell. Next, we will derive the propagation mechanism of tendon tension.

Fig. 3(d) displays the force analysis of the i-th to $(i+1)$-th cells. Fig. 3(c) displays a partial enlargement of the contact area between the tendon and the spring. As the tendon tension decays in the opposite direction of the velocity, the normal force and friction force also gradually decrease. Therefore, the direction of the normal force resultant force received by the tendon is not along the radial direction of the backbone, but deflected by an angle δ in the velocity direction. It is difficult to determine δ due to the complex force state of the contact surface. Therefore, unlike the conventional assumption where the normal force on the tendon is simplified to be along the plane of the spine [13], [14], the directions of the normal force and friction are relaxed in this modeling. Assuming A2, the friction coefficient is μ. The normal force and friction force at each point in the contact area have the same ratio μ and are perpendicular to each other. According to the cosine theorem, their resultant normal force and resultant friction force also have the same ratio μ and are perpendicular to each other. The i-th normal force is F_{Ni}, and the friction is written as:

$$f_i = \mu F_{Ni}\mathrm{sign}(s') \tag{8}$$

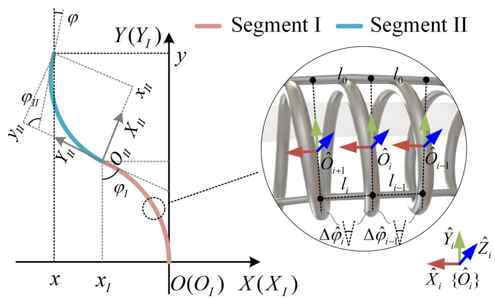

Fig. 4. Kinematic analysis.

where f_i is the friction at the i-th contact point, s' represents the tendon movement velocity. The resultant force of friction and normal force is calculated as:

$$F_c = \sqrt{F_{Ni}^2(1+\mu^2)}. \tag{9}$$

The resultant force of T_i and T_{i+1}, together with F_c, constitute the interaction force. The two are equal in size and opposite in direction, as shown in Fig. 3(d). By geometrically analyzing the i-th cell, we determine that the angle between the line connecting the two vertebrae midpoints and the end direction is $\frac{\varphi_i}{2}$. The angle between T_i and T_{i+1} is $(\pi - \frac{\varphi_i+\varphi_{i+1}}{2})$. Using the cosine theorem:

$$F_{Ni}^2(1+\mu^2) = T_i^2 + T_{i+1}^2 - 2T_iT_{i+1}\cos(\frac{\varphi_i+\varphi_{i+1}}{2}). \tag{10}$$

Assuming A1, the tension of the $(i+1)$-th cell is written as:

$$T_{i+1} = T_i - f_i. \tag{11}$$

Combining (1), (4), (8), (10), (11), we obtain an expression of the normal force F_{Ni} with respect to the tension T_i:

$$F_{Ni}^2 = 2T_i^2 - 2\mu T_i F_{Ni} - 2(T_i^2 - \mu T_i F_{Ni})\cos\left[\frac{D_0 l_0}{EI}(T_i - \frac{\mu F_{Ni}}{2})\right]. \tag{12}$$

Eq. (12) is the improved tendon tension propagation model, which is an implicit recursive form. Given the input tension T_0, the numerical solution of the normal force and friction at the first cell can be calculated. Based on assumptions A1 and A4, the forces and deformations of all subsequent cells are obtained step by step.

IV. Kinetostatic Modeling

A. Forward Kinematic Modeling

The kinetostatic model is derived based on the continuum morphology estimation model. Different from the PCC assumption, the kinetostatic model in this paper is established cell by cell. A quasi-static profile of the central axis is shown in Fig. 4. The coordinate system XOY is established with the starting point of segment I as the origin. Assume that the endpoint of segment I is (x_I, y_I) and the bending angle is φ_I. The local coordinate system $X_{II}O_{II}Y_{II}$ is established with the end point of segment I as the origin. In $X_{II}O_{II}Y_{II}$, the coordinate of the end of segment II is (x_{II}, y_{II}) and the bending angle is φ_{II}. The robotic system has an independent Y-axis DoF, so the Y-axis coordinate of the catheter tip is not considered here. Then the catheter tip pose is written as:

$$\begin{cases} x = x_I + (y_{II} - \frac{x_{II}}{\tan(\varphi_I)})\sin(\varphi_I) \\ \varphi = \varphi_I + \varphi_{II} \end{cases}, \tag{13}$$

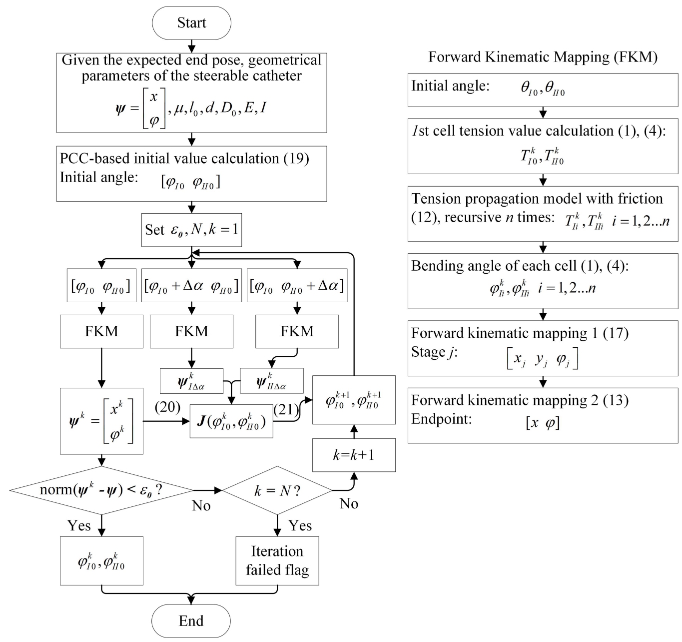

Fig. 5. Inverse kinematics numerical solution method.

where the positive bending direction is clockwise. Both segments' poses are functions of tendon displacement. The end of segment j is expressed as:

$$\begin{bmatrix} x_j \\ y_j \\ \varphi_j \end{bmatrix} = \mathbf{T}_j(\Delta p_j), \tag{14}$$

where $j = \{I, II\}$, $\mathbf{T}_j(\Delta p_j)$ represents the kinematic transformation matrix. Each segment is divided into 40 cells. Taking segment I as an example, local coordinate systems $\{\hat{O}_{i-1}\}$, $\{\hat{O}_i\}$, and $\{\hat{O}_{i+1}\}$ are established at the starting points of the $(i-1)$-th to $(i+1)$-th cells shown in Fig. 4. Their origins are located on the axis of the spring. The end point of the cell is the origin of the next cell. Assume that the continuum deforms in the plane. The end point of the i-th cell is written as:

$$\begin{bmatrix} x_i \\ y_i \end{bmatrix} = \begin{bmatrix} x_{i-1} \\ y_{i-1} \end{bmatrix} + \mathbf{R}_{i-1} \cdot \mathbf{P}_i, \tag{15}$$

where $\mathbf{R}_{i-1}$ is the rotation matrix from $i-1$-th to i-th:

$$\mathbf{R}_{i-1} = \begin{bmatrix} \cos(\varphi_{i-1}) & \sin(\varphi_{i-1}) \\ -\sin(\varphi_{i-1}) & \cos(\varphi_{i-1}) \end{bmatrix}, \tag{16}$$

where $\varphi_n = \sum_{i=1}^{n} \Delta\varphi_i$. $\mathbf{P}_i$ is the coordinate of the i-th cell end in $\{\hat{O}_i\}$, $\mathbf{P}_i = \begin{bmatrix} \hat{x}_i \\ \hat{y}_i \end{bmatrix}$. Then the pose of the catheter tip is:

$$\begin{bmatrix} x_I \\ y_I \\ \varphi_I \end{bmatrix} = \begin{bmatrix} x_0 \\ y_0 \\ \varphi_0 \end{bmatrix} + \begin{bmatrix} \sum_{i=1}^{n} (\mathbf{R}_{i-1} \cdot \mathbf{P}_i) \\ \sum_{i=1}^{n} (\varphi_i) \end{bmatrix}, \tag{17}$$

where $n = 40$. The mapping from the drive space to the task space for segment I is described by (17). The kinematic mapping of segment II is the similar to that of segment I. Finally, the poses of the catheter tip is obtained based on (13).

B. Inverse Kinematic Modeling and Numerical Solution

Based on the geometric analysis, the tendon displacement in the segment j is calculated by:

$$\Delta p_j = D_0 \varphi_j. \tag{18}$$

The goal of inverse kinematics modeling is establish a mapping from the motion space (x, φ) to the drive space (Δp_I, Δp_{II}). Since the obtained tendon tension propagation model is an implicit nonlinear recursive form, it is challenging to calculate the inverse kinematic analytical solution. In this paper, a model-based numerical solution method is designed to approximate the correct inverse solution. The flow chart is shown in Fig. 5. The 1-st cell bending angles of the two segments obtained by the PCC assumption are set as the initial values of the iteration:

$$\begin{cases} x = \frac{nl_0}{\varphi_{II}}(1-\cos\varphi_{II})\cos\varphi_I + \frac{nl_0}{\varphi_{II}}\sin\varphi_{II}\sin\varphi_I + \frac{nl_0}{\varphi_I}(1-\cos\varphi_I) \\ \varphi = \varphi_I + \varphi_{II} \end{cases} \tag{19}$$

To calculate the Jacobian matrix, the initial matrix elements are increased by a small increment $\Delta\alpha$. Based on the forward kinematics mapping (FKM), the catheter tip poses in the three input initial matrices are calculated, and the Jacobian matrix is calculated as:

$$\boldsymbol{J}(\mathbf{p}^k) = \begin{bmatrix} \frac{\partial f_1}{\partial \varphi_{I0}^k} & \frac{\partial f_1}{\partial \varphi_{II0}^k} \\ \frac{\partial f_2}{\partial \varphi_{I0}^k} & \frac{\partial f_2}{\partial \varphi_{II0}^k} \end{bmatrix}, \tag{20}$$

where $\mathbf{p}^k = \begin{bmatrix} \varphi_{I0}^k \\ \varphi_{II0}^k \end{bmatrix}$, f_1, f_2 are functions of variable $\mathbf{p}^k$, i.e. $x^k(\mathbf{p}^k)$, $\varphi^k(\mathbf{p}^k)$. When the tip pose error is less than a expected value ε_0 or reaches the maximum number of iterations N, the iteration ends. The expected position error is set to 0.1 mm, and the expected orientation error is set to 0.5°. The 1-st cell bending angle of the $(k+1)$-th iteration is obtained by solving the following equation:

$$\psi^{k+1} = \psi^k + J(\mathbf{p}^k)\cdot(\mathbf{p}^{k+1} - \mathbf{p}^k). \tag{21}$$

where $\psi = \begin{bmatrix} x \\ \varphi \end{bmatrix}$. Set the specific poses in 3D space: (a,b,c)=(20, 20, 80) mm, φ=[-45°, 0°, 45°, 90°]. Solve each pose and interpolate 20 nodes. Some central curves are shown in Fig. 6(a1-a4). Since the backbone is not on the continuum axis, the length of the central curve changes slightly as it bends, which is accounted for in the calculations. The workspace of the catheter tip is defined as the range of orientation angles that can be reached at a given offset. The dexterity is defined as the ratio of the angle range to 2π at a given offset [16]. The workspace the catheter tip with two bending DoFs and a axial rotation is shown in Fig. 6(b), where the bending angle of the each segment is less than 150°. The results show that the radial offset range of the catheter tip is $[-60, 60]$ mm, and the orientation angle covers $[-180, 180]°$. The dexterity is depicted in Fig. 6(c). Within the radial offset range of $[-50, 50]$ mm, the dexterity exceeds 0.5, that is, the controllable orientation angle range exceeds 180°. When the radial offset is within the range of $[-45, -30]$ mm and $[30, 45]$ mm, the dexterity is the largest and the controllable orientation angle range is 210°.

V. Experimental Validation

Fig. 7 displays the developed TDSCR. It mainly includes a steerable catheter, a tendon actuator, a PG2 gripper [15], and a leader side manipulator [17]. The OD of the stainless steel spring is 1.4 mm, the pitch is 1 mm, and the length of the catheter is 72.6 mm. The backbone diameter of the distal segment is 0.1 mm and the tendon is a stainless steel wire. The backbone diameter of the proximal segment is 0.15 mm and the tendon is a smooth PTFE tendon sheath. When welding, straighten the spine and spring axis in advance and keep them as coaxial as possible. Through the cantilever beam free end load tests, the measured bending stiffness of the catheter segment I is $11.793\times10^{-6}\mathrm{N\cdot m^2}$ and that of segment II is $5.347\times10^{-6}\mathrm{N\cdot m^2}$. The total length of the catheter is 0.5 m. The upper part of Fig. 7 shows a catheter prototype with a sub-millimeter OD of 0.96 mm. The tendon and tendon sheath are pulled and pushed by the tendon actuator. The right side of Fig. 7 displays the leader side manipulator designed by us previously [17]. It can accurately collect the operator's clamping, twisting, pushing and pulling information. The enlarged view shows the incremental design for operating the steerable catheter. Two encoders measure the expected offset displacement and orientation respectively. The motion of the steerable catheter is collected by a camera. A dual-mode control strategy is proposed to enable navigation in both

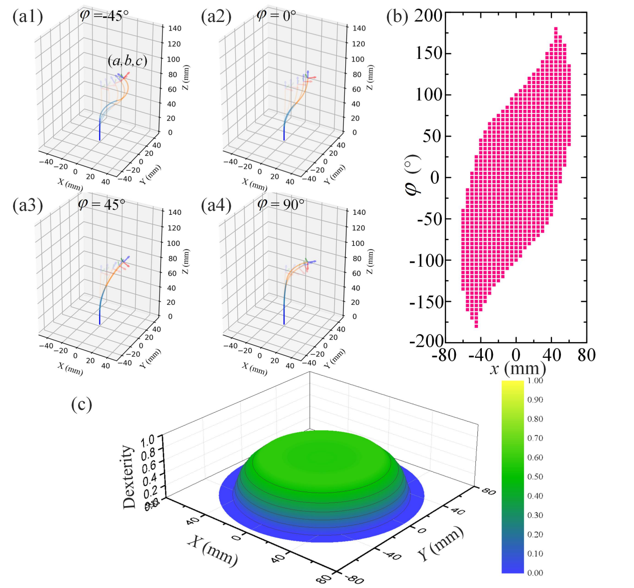

Fig. 6. Workspace and dexterity. (a) (a,b,c)=(20,20,80) mm, (a1) φ=-45°, (a2) φ=0°, (a3) φ=45°, (a4) φ=90°. (b) Workspace. (c) Dexterity.

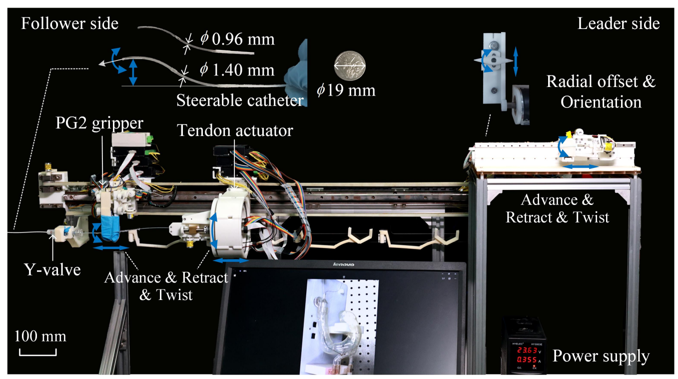

Fig. 7. The developed TDSCR. The operator controls the steerable catheter through the leader-follower system, including grasping, advancing, retracting, twisting, and adjusting the pose of the tip.

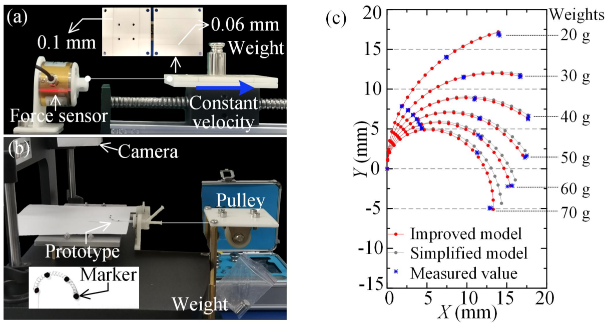

Fig. 8. Experimental validation of the improved tendon tension propagation model. (a) Friction coefficient measurement experiments on continuum prototypes. (b) Experimental setup. (c) Experimental results.

unrestricted and confined spaces. Mode I activates the distal and proximal segments. Based on the kinetostatic model, the position and orientation of the catheter tip can be accurately controlled. It is used for navigation in wide spaces, which is also the focus of this paper. In narrow spaces, the entire proximal segment is confined and active bending results in significant contact forces. Therefore, mode II only activates the distal segment to adjust the orientation of the catheter tip. The operator switches between the two modes according to the type of working environment.

A. Experimental validation of the improved tendon tension propagation model

To demonstrate the effectiveness of the improved tendon tension propagation model, single-segment continuum bending experiments are performed. To highlight the results difference between the improved model and the simplified model [13], [14], we fabricated a stainless steel continuum prototype with the following parameters: D_0=1.4 mm, d_0=0.1 mm, tendon diameter 0.06 mm, spring wire diameter 0.15 mm, pitch 1.25 mm, and 20 turns. An experimental setup for measuring the friction coefficient of the tendon friction pair is built, as shown in Fig. 8(a). Two stainless steel wires with diameters of 0.06 mm and 0.1 mm are respectively wound around two flat plates, and then the two wires are stacked together at 90° to simulate the contact state between the tendon and the spring. The normal force between the steel wires is adjusted by weights. The lower plate is pulled by the screw platform at a constant velocity, and the friction between the two steel wires is measured by a force sensor. Based on Coulomb's law of friction, the measured friction coefficient is 0.352. A tendon tension propagation model experimental setup is built, as shown in Fig. 8(b). The root of the prototype is fixed on the base, and the tendon is connected to a weight by passing through a fixed pulley. The weights are set to 20 g, 30 g, 40 g, 50 g, 60 g, and 70 g. Four circular black markers are attached to the prototype and detected by a camera. For each weight, the experiment is repeated 3 times, and the results are displayed in Fig. 8(c). The experimental results indicate that, with the bending angle increasing, the estimation error of the simplified model grows gradually, while the improved model retains low error. When the weight is 70 g, the mean absolute error (MAE) of the end position of the simplified model is 1.54 mm, and the MAE of the improved model is 0.43 mm.

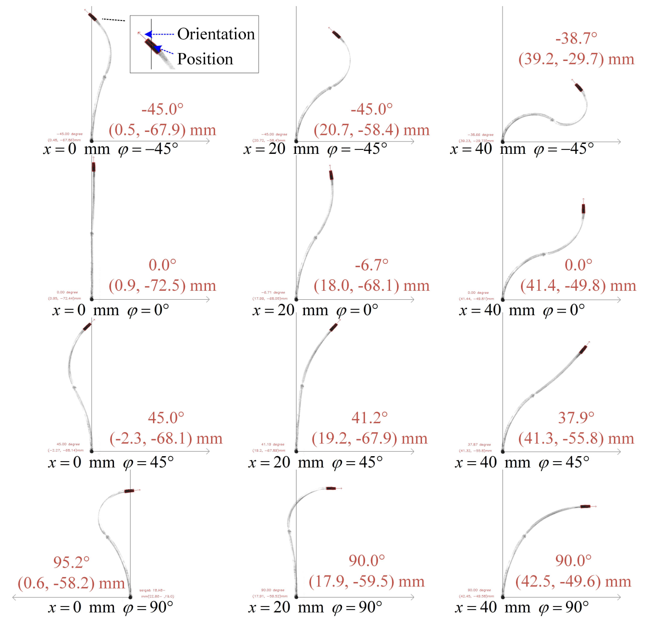

Fig. 9. Experimental results of catheter tip pose control. Red fonts represent measured poses, and black fonts represent expected poses.

The results demonstrate that the improved tension propagation model has better estimation accuracy, especially in the case of large deformation.

B. Pose Control Experiment

Pose control experiment in wide space is conducted to evaluate the feasibility and control accuracy of the steerable catheter. The catheter tip is set to 20 poses with the position and orientation of the gradient. The position range is $x\in$[0, 40] mm and the angle range is $\varphi\in$[-45°, 90°]. The displacements of the tendons are iterated based on the kinematics model. The model is iterated on an AMD Ryzen 7 4800H 2.9GHz CPU, taking 94 ms per pose. The solutions are input into the tendon actuator. The stabilized catheter poses recorded by a camera. When the catheter is advanced or retracted, the deformation of the passive section of the catheter will interfere with the lateral offset of the tip, so the catheter is fixed axially in the experiment. 3 repetitive experiments are conducted for each pose. The results are shown in Fig. 9 and TABLE I. It indicates that the position MAE of the proposed model is 1.44 mm, and the angle MAE is 2.63°. The maximum position and orientation errors are 3.9 mm and 7.1°. They occur at x=30, 40 mm and φ=45°. The reason can be that the small input is disturbed by the return error of the distal tendon. Further, two experiments are conducted with the simplified model and PCC model as control groups, where the PCC model considers the two segments as two arcs. Experimental results are dispalyed in TABLE I. It shows that the proposed model improves the position accuracy by 46.5% and the orientation accuracy by 57.6% compared with the simplified model, and by 72.7%, 83.0% in these metrics compared with the PCC model.

C. Path Following Experiment

To evaluate the leader-follower control performance of the TDSCR, a path following experiment is performed. The path

This article has been accepted for publication in IEEE Robotics and Automation Letters. This is the author's version which has not been fully edited and content may change prior to final publication. Citation information: DOI 10.1109/LRA.2025.3588417

TABLE I
EXPERIMENTAL RESULTS OF THE TIP POSE CONTROL

Methods	Repetition	x(mm)					φ(°)			
		0	10	20	30	40	-45	0	45	90
PCC	1	-0.3	7.4	15.2	22.6	31.2	-33.9	-2.9	24.6	57.8
	2	-1.1	7.2	15.2	22.3	30.9	-31.5	0.5	28.1	60.3
	3	-0.9	7.3	15.5	22.3	30.9	-31.5	0.5	28.8	61.4
	MAE			5.25				15.51		
Simplified model [14]	1	0.9	9.5	18.3	27.4	36.8	-38.5	1.6	41.0	76.6
	2	0.4	9.1	18.4	27.8	36.8	-39.2	0.8	40.7	79.0
	3	0.4	10.0	18.3	27.8	36.5	-40.3	1.2	42.3	78.6
	MAE			2.69				6.21		
This paper	1	-0.4	9.7	19.0	31.1	41.1	-42.9	-1.3	42.4	87.8
	2	-1.1	8.5	18.0	30.7	41.0	-43.2	-1.4	41.6	86.3
	3	-0.9	10.0	19.5	31.1	41.4	-41.8	-1.6	42.0	86.6
	MAE			**1.44**				**2.63**		

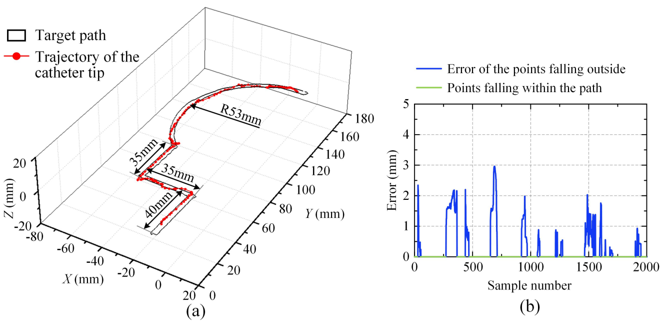

Fig. 10. The operator manipulates the steerable catheter following a path. (a) Results of the catheter tip following the path. (b) Following error.

is shown in the black line in Fig. 10. It includes three straight lines with lengths of 40, 35, and 35 mm, respectively, and an arc path with a radius of 53 mm and a central angle of 135°. The total length of the path skeleton is 235 mm, and the path width is less than 3 mm. The operator remotely manipulated the steerable catheter along the path. The catheter following state was observed and adjusted along the narrow path. The total operation time is 140 s. The experiment results are shown in Fig. 10(a). The red dot represents the trajectory of the catheter tip. Employing the ray casting method, the number of points falling within the path area accounted for 78.2%, as shown in Fig. 10(b). The MAE of the points falling outside the area is 1.15 mm, and the maximum error is 2.96 mm. The results indicate that the operator can accurately control the catheter tip position remotely. By twisting the catheter, the workspace can be expanded into three dimensions.

D. Crossing Rings Experiment

To validate the navigation ability in a wide space, the catheter crossing sequence rings experiment is performed, as shown in Fig. 11(a). Rings with varying heights are employed, including 55, 70, 80 mm. The inner diameter of the rings is 8 mm, and they are fixed on a plane with a spacing of 65 mm. In the experiment, the operator remotely manipulated the catheter to actively bend and pass through each ring one by one. To demonstrate the dexterity of the steerable catheter, the Ring 2, Ring 3, and Ring 4 are rotated clockwise by 50°, 30°, and 50° respectively. It should be noted that the lateral offset between adjacent rings and the rotation along the offset direction reduces overlapping area of the two entrances. The overlapping area of the Ring 2 and Ring 1 is reduced by

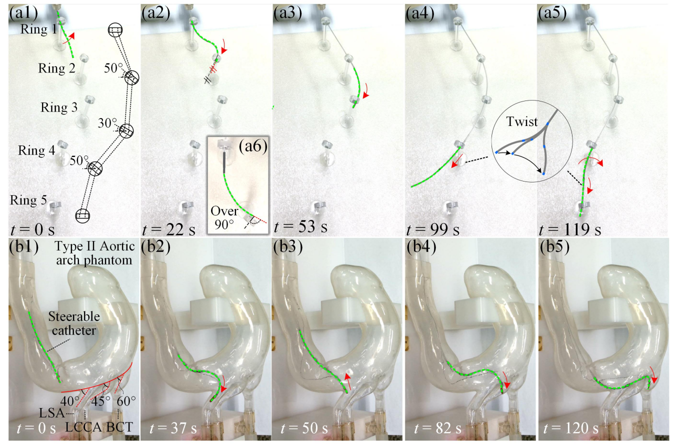

Fig. 11. Demonstration of dexterous navigating capabilities. (a1-a5) Steerable catheter crosses a set of rings. (a6) The tip pose of a single-actuator continunm is not decoupled and thus cannot enter Ring 2. (b1-b5) The catheter completed 3 carotid branch superselections.

82.3%, which significantly increased the difficulty of passing through the Ring 2. The task is challenging for the continunm whose position and orientation cannot be decoupled, such as single-DoF continuum and magnetic continuum. As shown in Fig. 11(a6), when the single-segment continuum moved to Ring 2, the angle between it and the axis of Ring 2 exceeded 90°, causing it to be unable to enter Ring 2. The operator accomplished the task smoothly using the proposed steerable catheter. As the catheter approached Ring 2, The operator controlled the catheter to make an ”S” turn. The catheter tip was moved along the ring offset direction, and the orientation was adjusted to be consistent with the axial direction of Ring 2. Then, the catheter entered Ring 2 without collision. The catheter tip enters the target channel without collision, indicating the dexterous control performance of the steerable catheter. Fig. 11(a3-a5) displays the catheter passed through the remaining rings. The whole task takes 119 s.

E. Carotid Artery Superselection Experiment

Even for surgeons with skills, superselection of three carotid arteries in a short time is a challenging task, especially for type II and III branches. Fig. 11(b) shows a type II aortic phantom. The angles between the LSA, LCCA, and BCT branches and the aortic arch are 40°, 45°, and 60°, respectively. In the experiment, the operator manipulated the catheter to complete the superselection of the LSA, LCCA, and BCT branches. The operator first twisted the catheter until the motion plane was basically consistent with the target branch. Then the operator adjusted the tip position close to the entrance of target branches and its orientation consistent with the each branch axis. Finally, the catheter was inserted into the target branches, as shown in Fig. 11(b2,b4,b5). The whole task takes 120 s.

F. Coronary Artery Superselection Experiment

Superselection experiment in a coronary artery phantom is conducted to validate the navigation capability in narrow environments. The coronary arteries are tortuous and complex, so the task is skillful and risky. Fig. 12 displays the coronary

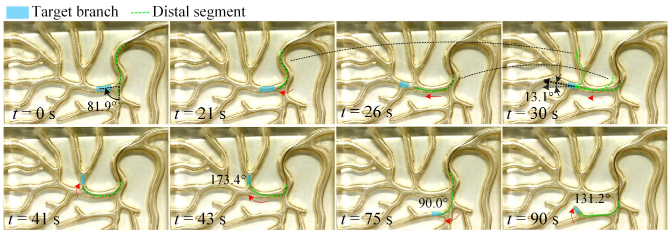

Fig. 12. Demonstration of navigating in narrow environment through a coronary artery phantom. The steerable catheter is activated with Mode II.

artery phantom made of glass. The blue area represents the target branch. The first target branch angle is 81.9°. The catheter is activated with Mode II. The operator bended the catheter tip sharply toward the target orientation and then inserted the catheter. The tip naturally moved toward the branch, allowing the catheter to enter the branch smoothly. In this process, the operator did not adjust the tendon displacement, and the tip orientation remained well (between t=21 s to t=30 s). The bending angle of the catheter is the sum of the angles of each chain cell. When the tendon is in tension, the comprehensive bending angle is controlled by tendon displacement, while the angles of each cell are redistributed based on the force interaction state with the environment. The property enables the catheter to adapt compliantly to tortuous vessels, reducing the difficulty of manipulation. The next target branch has a orientation angle of 173.4°. The operator withdrew the catheter close to the branch and further bent the tip, and thus successfully inserted the large angle branch (between t=30 s to t=43 s). The catheter also entered two deeper branches with orientation angles of 90.0° and 131.2° respectively (between t=43 s to t=90 s). Experimental results demonstrate that the steerable catheter, activated with Mode II, can adaptively adjust its shape according to the environment and has the ability to navigate efficiently in narrow blood vessels.

VI. Conclusion

To address the issue of low dexterity of existing vascular intervention catheters, we design a 4 DoFs TDSCR with decoupled control of the tip position and orientation. To this aim, a helical spring-based continuum is designed and two segments are combined to enable the end position and orientation control while maintaining miniaturization. To accurately estimate the continuum morphology, the lumped parameter model is constructed based on the chained beam model and a tendon tension propagation model considering the path friction is derived. The quasi-static continuum morphology is modeled cell by cell. Subsequently, based on the morphology estimation model, the kinetostatic model is established and a model-based numerical solution method is designed. The average iteration time for each pose is 94 ms. The calculated results indicate that, within the radial offset range of $[-50, 50]$ mm, the dexterity exceeds 0.5, that is, the controllable orientation angle range exceeds 180°.

The improved tension propagation model validation experiment and 20 tip poses control experiments are conducted. The results indicate that the tip position MAE of the proposed model is 1.44 mm and the orientation MAE is 2.63°, which is significantly higher than that of the traditional model. It demonstrates that the proposed model improves the morphological estimating and motion control accuracy, especially in the case of large deformation and multiple segments in series. Finally, path following, rings crossing, carotid artery and coronary artery superselection experiments in phantom are performed separately. The results demonstrate the superior flexibility and operability of the proposed TDSCR. It has the potential to reduce surgical difficulty and improve success rate and efficiency. In the future, we will further increase the length of the catheter to meet the requirements of standard surgery and consider the impact of physiological motion on the robust performance of catheter manipulation. The problems of reduced control accuracy and motion lag caused by longer catheters can be improved by reducing the gap between moving parts and using materials with large axial-bending stiffness ratio. Then leveraging X-ray images, we plan to employ it for in *vivo* experiments.

References

[1] X. Bao, S. Guo, Y. Guo *et al.*, “Multilevel operation strategy of a vascular interventional robot system for surgical safety in teleoperation,” *IEEE Trans. Robot.*, vol. 38, no. 4, pp. 2238–2250, 2022.

[2] H. Liu *et al.*, “Morphological features of normal aortic arch,” *Tianjin Med J.*, vol. 45, no. 4, pp. 397–401, 2017.

[3] M. Muneeb, N. Nuzhat *et al.*, “Assessment of the dimensions of coronary arteries for the manifestation of coronary artery disease,” *Cureus*, vol. 15, no. 10, 2023.

[4] J.-L. Wu, L. Zhang, J.-T. Qiu, and C.-T. Yu, “Morphological features of the thoracic aorta and supra-aortic branches in patients with acute type a aortic dissection in china,” *Interactive CardioVascular and Thoracic Surgery*, vol. 27, no. 4, pp. 555–560, 2018.

[5] W. Ba, X. Dong *et al.*, “Design and validation of a novel fuzzy-logic-based static feedback controller for tendon-driven continuum robots,” *IEEE ASME Trans. Mechatron.*, vol. 26, no. 6, pp. 3010–3021, 2021.

[6] Q. Peyron and J. Burgner-Kahrs, “Stability analysis of tendon driven continuum robots and application to active softening,” *IEEE Trans. Robot.*, 2023.

[7] S. Wei, Z. Wu, and J. Zhang, “Multimodal motion control of magnetic continuum robot for endovascular intervention navigation,” *IEEE/ASME Transactions on Mechatronics*, 2025.

[8] Y. Kim *et al.*, “Telerobotic neurovascular interventions with magnetic manipulation,” *Sci. Robot.*, vol. 7, no. 65, p. eabg9907, 2022.

[9] T. Zhang *et al.*, “Pneumaoct: Pneumatic optical coherence tomography endoscopy for targeted distortion-free imaging in tortuous and narrow internal lumens,” *Sci. Adv.*, vol. 10, no. 35, p. eadp3145, 2024.

[10] E. Nicotra *et al.*, “A soft micro-robotic catheter for aneurysm treatment: A novel design and enhanced euler-bernoulli model with cross-section optimization,” in *2024 IEEE Int. Conf. Robot. Autom. (ICRA)*. IEEE, 2024, pp. 11 585–11 591.

[11] Y. Cao, W. Yang, S. Wang, S. He, Z. Liu, and L. Xie, “Improved trajectory tracking control for a continuum robot using error-driven adrc with input mapping method,” *IEEE Trans. Ind. Electron.*, 2024.

[12] P. Daemi *et al.*, “Development and evaluation of a friction model for tendon-driven soft robotic devices,” *IEEE Trans. Med. Robot. Bionics.*, vol. 5, no. 2, pp. 429–441, 2023.

[13] H. Yuan, L. Zhou, and W. Xu, “A comprehensive static model of cable-driven multi-section continuum robots considering friction effect,” *Mechanism and Machine Theory*, vol. 135, pp. 130–149, 2019.

[14] T. Kato, I. Okumura, S.-E. Song, A. J. Golby, and N. Hata, “Tendon-driven continuum robot for endoscopic surgery: Preclinical development and validation of a tension propagation model,” *IEEE ASME Tran. Mechatron.*, vol. 20, no. 5, pp. 2252–2263, 2014.

[15] Y. Yan, S. Guo, Z. Lin, C. Lyu, D. Zhao, P. Yang, Y. Zhang, Y. Zhang, and J. Liu, “Grasping-force-based passive safety method for a vascular interventional surgery robot system,” *IEEE Transactions on Instrumentation and Measurement*, vol. 72, pp. 1–12, 2023.

[16] X. Ai *et al.*, “Dexterity comparison and analysis of multi-contact-aided continuum manipulators,” *IEEE Robot. Autom. Lett.*, 2024.

[17] Y. Yan, S. Guo *et al.*, “A novel sea-based haptic interface for robot-assisted vascular interventional surgery,” in *2024 IEEE Int. Conf. Robot. Autom. (ICRA)*. IEEE, 2024, pp. 5871–5876.